Available online at www.sciencedirect.com

ScienceDirect

Geochimica et Cosmochimica Acta 323 (2022) 202–219

Geochimica et Cosmochimica Acta

www.elsevier.com/locate/gca

Chemical study of group IIIF iron meteorites and the potentially related pallasites Zinder and Northwest Africa 1911

Bidong Zhang [a,*], Nancy L. Chabot [b], Alan E. Rubin [a,c], Munir Humayun [d], Joseph S. Boesenberg [e], Deon van Niekerk [f]

[a] *Department of Earth, Planetary & Space Sciences, University of California, Los Angeles, CA 90095-1567, USA*
[b] *Johns Hopkins University Applied Physics Laboratory, Laurel, MD 20723, USA*
[c] *Maine Mineral & Gem Museum, 99 Main Street, P.O. Box 500, Bethel, ME 04217, USA*
[d] *National High Magnetic Field Laboratory and Department of Earth, Ocean & Atmospheric Science, Florida State University, Tallahassee, FL 32310, USA*
[e] *Earth, Environmental and Planetary Sciences, Brown University, Providence, RI 02912, USA*
[f] *Department of Geology, Rhodes University, Makhanda 6140, South Africa*

Received 31 March 2021; accepted in revised form 2 February 2022; Available online 10 February 2022

Paper dedicated to the memory of Prof. John T. Wasson.

Abstract

Group IIIF was established as a magmatic iron-meteorite group based on similar Ga and Ge abundances, unusually high Ga/Ge ratios, and the IIIAB-like interelement trends in its members; recent Mo and Ru isotopic data indicate that three of its members exhibit the isotopic signature of carbonaceous-chondrite (CC) irons. Here we report the elemental chemistry of this group and model its crystallization history. Included are new elemental data for IIIF irons acquired by both instrumental neutron activation analysis (INAA) and laser ablation inductively-coupled plasma mass spectrometry (LA-ICP-MS). A fractional-crystallization model was used to evaluate the IIIF compositional trends for 19 elements and was unable to explain the observed fractionation trends for several key elements (Co, Ga, Ge). In particular, the inability of this model to match Co in the IIIF irons is striking because (1) group IIIF has the widest Co variation among all magmatic iron groups and (2) none of the tested initial S contents (0–20 wt.%) explains both the wide Co variation and steep Co-As slope. Attempts to fit subsets of the IIIF irons were also unsuccessful. In addition, group IIIF has the greatest variety of structural classes and kamacite bandwidths among all established magmatic iron groups. If the IIIF irons constitute a coherent group, they were derived from a parent body that experienced more complex processes than simple fractional crystallization of the core.

The Zinder and Northwest Africa (NWA) 1911 pyroxene-bearing pallasites were recently suggested to be related to group IIIF based on their Ga and Ge contents, and we completed a petrographic study of the pallasite silicates and LA-ICP-MS analyses of their metal fractions. The two pallasites are related to one another: they have nearly identical mineralogical, elemental and O-isotopic compositions in their silicates and metals. Their metallic compositions resemble those of the IIIF irons Moonbi, St. Genevieve County, and Cerro del Inca, but their O-isotopic compositions resemble those of non-carbonaceous (NC) achondrites. Additional isotopic measurements are needed to test the potential genetic relationship to group IIIF.

* Corresponding author.
E-mail address: bdzhang@ucla.edu (B. Zhang).

https://doi.org/10.1016/j.gca.2022.02.004

Keywords: Iron meteorite; Group IIIF; Pallasite; Fractional crystallization; Neutron activation analysis; Inductively coupled plasma mass spectrometry

1. INTRODUCTION

Magmatic iron meteorites are thought to represent the cores of differentiated asteroids (e.g., Scott, 2020). Group IIIF was first defined as a group based on distinct ranges of Ga (6.3–7.2 ppm) and Ge (0.7–1.1 ppm) (Scott and Wasson, 1976). Because IIIF irons have element vs. Ni correlations similar to those of other magmatic groups (Kracher et al., 1980), they are thought to have formed via fractional crystallization of a metallic core. Nickel, Ga, Ge, Ru, Re, Os, Pt, Ir, and Au concentrations in the IIIF irons (determined by radiochemical neutron activation analysis, RNAA) have previously been reported (Schaudy et al., 1972; Scott and Wasson, 1976; Kracher et al., 1980; Pernicka and Wasson, 1987). New highly-siderophile-element (HSE, Re, Os, Ir, Ru, Pt, and Pd) data determined by inductively coupled plasma mass spectrometry (ICP-MS) were reported by Hilton et al. (2021).

According to the Meteoritical Bulletin Database, group IIIF currently has nine members (all finds): Binya, Cerro del Inca, Clark County, Fitzwater Pass, Klamath Falls, Moonbi, Nelson County, Oakley (iron), and St. Genevieve County. Table 1 provides a summary of the petrography and metallography of these nine irons (Buchwald, 1975; Kracher et al., 1980). All IIIF members are octahedrites, with structures varying from fine to coarsest (Table 1). Schreibersite is common in several samples, occurring on the micrometer-to-millimeter scale. Troilite is present as millimeter-size crystals in Clark County, Nelson County, and Oakley (iron).

Hafnium-W chronometry of Nelson County suggests that mantle-core differentiation of its parent body (presumed to be that of group IIIF) occurred 1.5 ± 1.7 Ma after CAI formation (Qin et al., 2008), and a later estimate based on Clark County and Klamath Falls shows 2.2 ± 1.1 Ma (Kruijer et al., 2017). The Hf-W age of the IIIF irons has recently been revised to 3.0 ± 1.2 Ma due to the discovery of nucleosynthetic Pt isotope anomalies (Spitzer et al., 2021). Molybdenum and W isotopic measurements of Clark County and Klamath Falls show that they are carbonaceous-type (CC) irons (Kruijer et al., 2017). Additional Ru isotopic analyses of Clark County, Klamath Falls, and Oakley (iron) confirmed the CC classification (Worsham et al., 2019). The S-isotopic compositions of Moonbi, Cerro del Inca, and Klamath Falls show significant ^{33}S depletions relative to those of other iron-meteorite groups (Antonelli et al., 2014; Peters et al., 2020).

The metallic fractions of two pyroxene-bearing pallasites, Zinder and Northwest Africa (NWA) 1911, were reported to have elemental concentrations close to the IIIF

Table 1
Summary of the petrography and metallography of IIIF irons.

Sample	Find location	Structure‡	Kamacite bandwidth (mm)	Schreibersite	Modal P (wt.%)	Troilite	Modal S (wt.%)
Clark County	Kentucky, USA	Om	1.00 ± 0.10	25–50 μm nodules	0.05	3 × 1 mm lenses, shock melted	0.05§
Nelson County	Kentucky, USA	Ogg	1–10	rare, 2–30 μm wide lamellae	0.18	mm-scale lenticular or platy bodies	
Oakley (iron)	Idaho, USA	Og	1.40 ± 0.30	20–80 μm wide grain	0.28	irregular nodules, 50 μm to 5 mm	0.016¶
Binya	Australia	Og*	1.0–1.5*				
Cerro del Inca	Chile	Of–Om*	0.5*				
St. Genevieve County	Missouri, USA	Of	0.49 ± 0.07	10–60 μm wide grains and 2–40 μm blebs	0.22	monocrystalline	0.001#
Moonbi	Australia	Om	0.55 ± 0.10	0.2–0.6 mm skeletal crystals	0.22	not present	
Klamath Falls	Oregon, USA	Of†	0.5 ± 0.1†	more schreibersite than other IIIFs†			

Most information is from Buchwald (1975) otherwise labeled, and blank fields denote unreported data.
* Meteoritical Bulletin Database.
† Kracher et al. (1980).
‡ Of = fine octahedrite, Om = medium octahedrite, Og = coarse octahedrite, Ogg = coarsest octahedrite.
§ Cohen (1905).
¶ Merrill (1927).
# Moore et al. (1969).

irons, indicating a possible linkage of these pallasites with the IIIF parent body (Boesenberg et al., 2012; Boesenberg et al., 2017; Humayun et al., 2018). Only a few other pallasites have previously been linked to specific iron-meteorite groups, e.g., IIIAB and main-group pallasites (Wasson and Choi, 2003) and IIF and Eagle Station pallasites (Hilton et al., 2020). However, Humayun et al. (2018) found that the O-isotopic compositions of Zinder and NWA 1911 are similar to non-carbonaceous (NC) achondrites (see Section 4.6 for details), in contrast to the CC classification of IIIF irons derived from Mo, W, and Ru isotopes (Kruijer et al., 2017; Worsham et al., 2019). To date, no studies have modeled the crystallization of the IIIF core to investigate its possible genetic relationship to these two pallasites.

In this study, we report the first comprehensive elemental concentrations of group IIIF irons, using both instrumental neutron activation analysis (INAA) and laser ablation inductively coupled plasma mass spectrometry (LA-ICP-MS). We also report new siderophile-element data for the metal portions of the pallasites Zinder and NWA 1911 along with comprehensive petrographic studies of these meteorites. We undertake modeling to test if fractional crystallization can explain their interelement trends and whether the two pallasites are related to group IIIF.

2. ANALYTICAL METHODS AND RESULTS

2.1. Neutron activation analysis (NAA)

For each IIIF sample, Fe (for internal normalization) and 12 other elements in two to three specimens of a sample (from a single source) were analyzed by INAA. The methods are described in Wasson et al. (1989) and Wasson et al. (2007). The specimens have a mean thickness of 3.0 mm and a mass of ~550 mg. Samples were then irradiated at the University of California, Irvine nuclear reactor. After irradiation, each specimen was acid-leached using dilute H_2SO_4, HCl, and HNO_3 solutions to remove superficial contaminations. Each irradiated specimen was counted four times (6, 15, 80, and 600 hours, respectively, after the irradiation) on a hyperpure planar germanium detector over the course of a month at UCLA. Some sample-specific geometric corrections (0.95–1.05) to the Ni and Co values were made to be consistent with the third and fourth counts, in which Fe + Ni is corrected to be 990 mg/g. For analyses made in the last two decades, the standards used were a Filomena specimen of North Chile (IIAB), a Coahuila specimen (IIAB), and NBS steel NBS809B. In analyses prior to 1986, Filomena was not used as a standard; instead, aliquots of standardized solutions were used. Some of the older data were re-calculated by re-standardizing them by newer analyses; the recalculations make <5% difference. Except for the irradiation, all experimental procedures and data processing were performed at UCLA.

Concentrations of Ge were previously analyzed by radiochemical neutron-activation-analysis (RNAA) because Ge concentrations were below INAA detection limits. Therefore, the Ge RNAA data shown in this study are mainly from the literature (Schaudy et al., 1972; Scott

Table 2
Mean compositions of seven IIIF irons and one IIIF-an iron determined by NAA.

Meteorite	Cr (μg/g)	Co (mg/g)	Ni (mg/g)	Cu (μg/g)	Ga (μg/g)	Ge (μg/g)	As (μg/g)	Ru (μg/g)	W (μg/g)	Re (ng/g)	Os (μg/g)	Ir (μg/g)	Pt (μg/g)	Au (μg/g)
IIIF														
Clark County	313	3.13	69.3	96	6.70*	1.02*	1.22	6.5	1.81	805	10.1	7.57	8.2	0.325
Nelson County	326	3.10	70.6	91	6.31*	0.89*	1.25	7.8	1.68	942	12.9	8.87	9.6	0.311
Oakley (iron)	240	3.21	72.5	93	7.03†	1.13†	1.43		1.62	532		5.61	9.2	0.385
Cerro del Inca	291	3.79	76.9	174	6.17§	<50§	4.34		1.06	321		3.34	8.0	0.537
St. Genevieve County	359	3.83	77.1	170	6.35*	0.779*	4.60	4.86	1.02	185	2.1	2.00	8.1	0.598
Moonbi	215	3.86	81.6	189	6.64*	0.822*	5.74	5.32	1.07	140	1.0	1.41	8.1	0.710
Klamath Falls	30	4.86	87.3	169	7.05‡	0.701‡	23.9		0.39	<20		0.0050	2.3	3.238
IIIF-an														
Binya	192	4.17	76.7	112	9.48§	<65§	2.71		1.44	1174		9.59	10.9	0.513

* Ge data and one replicate of Ga from Schaudy et al (1972).
† Ge data and one replicate of Ga from Scott and Wasson (1976).
‡ Ge data and one replicate of Ga from Kracher et al. (1980).
§ Ga or Ge data analyzed solely by INAA.

and Wasson, 1976; Kracher et al., 1980), except for Binya and Cerro del Inca (determined by INAA in this study because Ge was not below detection). Gallium data were calculated from both our new INAA data (when available) and the RNAA data from the literature (Schaudy et al., 1972; Scott and Wasson, 1976; Kracher et al., 1980). The INAA data of group IIIF were collected over the past four-plus decades; starting in 1986, the data quality significantly improved. Except for two replicates of Klamath Falls, all other analyses were carried out after 1986 (see details in Appendix 1). For Klamath Falls, the specimen analyzed after 1986 was given 2× weight in the mean calculation. In the following sections, "NAA" refers to data derived from both INAA and RNAA, while "INAA" and "RNAA" denote data solely from INAA and RNAA, respectively.

The abundances of 14 elements determined by NAA are listed in Table 2, and replicate values of each specimen are shown in Appendix 1. The relative 95% confidence limits on the mean values in Table 2 are: 1.5–3% for Co, Ni, Ga, Ir (concentrations >0.1 μg/g) and Au; 4–6% for As, Ge (by RNAA) and Sb; 7–10% for W (values >0.3 μg/g), Re (>50 ng/g), Ru (>4 μg/g) and Pt (>2 μg/g). Chromium most commonly occurs in minor phases such as chromite and daubréelite, and such sampling bias induced high relative confidence limits (>10%) on the means of Cr. Moreover, Fe produces interference in the determination of Cr due to the $^{54}Fe(n,\alpha)^{51}Cr$ fast-neutron reaction. The degree of interference is about 6 μg Cr per gram of Fe (Wasson and Richardson, 2001). Our data were not corrected for this interference.

2.2. LA-ICP-MS

Samples of Cerro del Inca (museum number USNM 7062), Clark County (USNM 1304-a), Fitzwater Pass (CML 0413-6), Klamath Falls (USNM 7008-a and AMNH 4926-psl), Moonbi (USNM 1457-a), Nelson County (USNM 674-b), Oakley (iron) (USNM 780-d), and St. Genevieve County (USNM 454-a) were obtained as polished slabs. A mount of Zinder (~3 cm per side) was provided by Northern Arizona University. A small, 4 × 12 mm thin section of NWA 1911 was borrowed from the collection of Ted Bunch. Trace-element data on metals were collected by LA-ICP-MS at Florida State University (FSU).

LA-ICP-MS analyses were performed on an ElectroScientific Instruments New Wave™ UP193FX laser system coupled to a Thermo Element XR™ ICP-MS at the Plasma Analytical Facility, FSU. A low mass resolving power (ΔM/M = 400) and triple mode detection at 65% duty cycle were used to acquire the peaks ^{31}P, ^{51}V, ^{53}Cr, ^{55}Mn, ^{57}Fe, ^{59}Co, ^{60}Ni, ^{63}Cu, ^{71}Ga, ^{74}Ge, ^{75}As, ^{95}Mo, ^{102}Ru, ^{103}Rh, ^{106}Pd, ^{120}Sn, ^{121}Sb, ^{182}W, ^{185}Re, ^{190}Os, ^{193}Ir, ^{195}Pt and ^{197}Au. Irons were analyzed using a raster scan over a few millimeters with a 50 μm beam spot, scanned at 10 μm/s, 50 Hz laser repetition rate. This technique yielded more representative sampling of the kamacite-taenite banding but failed to yield useful Ge abundances for Klamath Falls. To obtain more precise Ge, a set of five 150 μm spots were analyzed at 50 Hz for 20 s on five of the irons, including

Table 3
Compositions (raster averages) of 23 elements in seven IIIF irons and two pallasites determined by LA-ICP-MS. Concentrations below detection limits are not shown.

Meteorite	P (mg/g)	V (μg/g)	Cr (μg/g)	Mn (μg/g)	Fe (mg/g)	Co (mg/g)	Ni (mg/g)	Cu (μg/g)	Ga (μg/g)	Ge (μg/g)	As (μg/g)	Mo (μg/g)	Ru (μg/g)	Rh (μg/g)	Pd (μg/g)	Sn (μg/g)	Sb (μg/g)	W (μg/g)	Re (μg/g)	Os (μg/g)	Ir (μg/g)	Pt (μg/g)	Au (μg/g)
IIIF																							
Nelson County	2.01	0.74	269	0.59	928	3.18	67	80	6.3	0.81	0.95	3.61	9.42	1.29	2.47	0.057	0.017	2.15	1.32	18.8	12.7	12.9	0.33
Clark County	1.50				923	3.27	73	73	6.8	0.78	0.97	5.88	8.50	1.27	2.86	0.057	0.007	2.15	0.85	11.8	8.82	11.4	0.38
Oakley (iron)	1.68				923	3.36	74	72	6.4	0.76	1.01	7.46	8.42	1.33	3.23	0.081	0.009	2.48	0.78	9.68	7.79	11.6	0.39
Cerro del Inca	5.90	1.05	291	1.43	916	3.69	73	111	6.2	0.61	3.01	17.1	8.60	1.31	3.16	0.257	0.036	4.39	0.405	3.81	4.20	10.2	0.49
St. Genevieve County	3.16				920	3.87	76	111	6.3	0.59	4.58	14.7	7.01	1.23	3.28	0.088	0.009	1.29	0.199	1.59	2.18	8.46	0.55
Moonbi	3.26	1.12	302	1.80	916	3.86	76	151	6.9	0.87	5.80	9.36	7.46	1.34	3.87	0.360	0.042	1.33	0.269	1.53	2.23	10.4	0.75
Klamath Falls	3.52	1.25	24	2.01	907	5.12	84	161	6.8	0.26*	25.8	6.10	2.00	0.96	5.55	0.436	0.040*	0.51	0.002*	0.003*	0.006*	1.97	3.33
Pallasite																							
Zinder	1.34	0.08	3	2.65	926	4.26	69	110	5.6	0.73	3.54	9.62	10.85	1.58	3.37	0.556	0.006	1.66	0.92	10.0	8.48	13.2	0.74
NWA 1911	2.18	1.50	29	18.55	907	4.12	77	132	6.1	1.11	5.29	6.09	9.83	1.57	3.72	0.77	0.06	1.43	0.69	8.58	7.48	12.9	0.90

* Data for Ge, Sb, Re, Os, Ir with lower detection limits are calculated from the mean of the spot average (Appendix 2) and the raster average in this table.

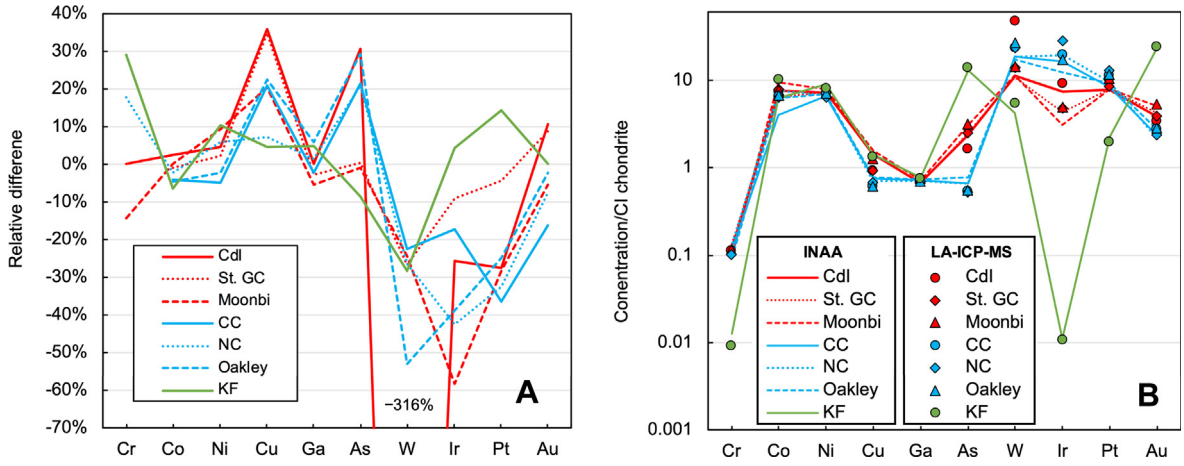

Fig. 1. Comparison between NAA and LA-ICP-MS data. A: relative difference between NAA and LA-ICP-MS. The relative difference is calculated using $(C_{NAA} - C_{ICPMS})/C_{INAA} \times 100\%$, where C denotes concentration data. B: NAA and LA-ICP-MS data normalized to CI chondrites. Abbreviations: St. GC for St. Genevieve County, CdI for Cerro del Inca, CC for Clark County, NC for Nelson County, KF for Klamath Falls. The CI-chondrite composition is from McDonough and Sun (1995). (For interpretation of the colors in the figure, the reader is referred to the web version of this article.)

both slabs of Klamath Falls. This produced a sufficiently bright beam to resolve Ge from background argide interferences. Standardization techniques followed those of Humayun (2012). The standard used for Fe, Co, Ni, Cu, Ga, Ge, As, W, and Au is North Chile (Filomena; IIAB) (Wasson et al., 1989), and the standard for Ru, Rh, Pd, Re, Os, Ir, and Pt is Hoba (IVB) (Walker et al., 2008). NIST SRM 1263a V-Cr steel was also used for V, Cr, Fe, Co, Ni, Cu, As, Mo, W, and Au (Campbell and Humayun, 2005). The abundances of the 23 elements determined by LA-ICP-MS raster averages taken on polished surfaces of IIIF irons are listed in Table 3 and spot averages in Appendix 2.

2.3. Comparison between NAA and LA-ICP-MS data

The elemental data from the NAA and LA-ICP-MS are compared by relative variations (Fig. 1A) and by absolute variations on the CI-chondrite-normalized diagram (Fig. 1B). The difference in data obtained by these two analytical methods mostly varies within the range of ±40% (LA-ICP-MS relative to NAA) (Fig. 1A). The largest divergence is in the W measurement of Cerro del Inca: 1.06 ng/g by INAA and 4.39 ng/g by LA-ICP-MS. The differences in Au and As between INAA and LA-ICP-MS go up to 30%, and this indicates that data from the larger sample size of NAA (minimizing the effects of variable kamacite/taenite sampling and/or local minor inclusions) are more suitable for fractional-crystallization modeling based on element-Au and element-As trends. For Ni, Co, and Ga that vary less in concentrations within a group, their concentrations measured by NAA and LA-ICP-MS are very comparable (difference within ±10%). Nevertheless, all measurements by NAA and LA-ICP-MS agree with each other on a logarithmic scale (Fig. 1B). Because the NAA specimens were larger, they would provide a more representative bulk measurement. Thus, for the composition of each IIIF iron used in the fractional-crystallization modeling of this study, we chose to use the elemental concentrations from NAA, and supplement those with the LA-ICP-MS measurements to extend the modeling to more elements. Given the consistent analysis values on the logarithmic scale between the two measurement approaches, the choice of using NAA or LA-ICP-MS values in the modeling made no significant difference in the conclusions.

2.4. Classification of Fitzwater Pass and Binya

Fitzwater Pass was previously classified as a IIIF member (As = 17.9 μg/g, Au = 1.8 μg/g, Ga = 10 μg/g, Ge < 10 μg/g, Ir = 2.54 μg/g) based on results from a commercial INAA lab (Meteoritical Bulletin Database). Fitzwater Pass has not been analyzed by NAA at UCLA. Our LA-ICP-MS analysis (As = 8.9 μg/g, Au = 1.36 μg/g , Ga = 79 μg/g, Ge = 301 μg/g, Ir = 3.12 μg/g) revealed higher abundances of Ga and Ge, but similar Ni, Co, As, Au, and Ir concentrations (see details in Appendix 3). If the piece of metal provided for this study was indeed Fitzwater Pass, then it is more compatible with group IAB than IIIF (Humayun et al., 2018). Binya is on the interelement trends of other IIIF irons, despite its slightly higher Co and Ga concentrations. We tentatively classify Binya as IIIF-an. Binya and Fitzwater Pass are excluded from the fractional-crystallization modeling of group IIIF.

2.5. Electron microprobe analysis (EMPA) and pallasite petrography

Quantitative analysis, mixed WDS/EDS element mapping, and characterization of the mineral phases from NWA 1911 and Zinder were performed on the Brown University CAMECA SX-100 electron microprobe.

Table 4
Mineral compositions of Zinder and NWA 1911 and other pyroxene-bearing pallasites. Data of Choteau, Vermillion, and NWA 10019 from Gregory et al. (2016), Boesenberg et al. (2000), and Boesenberg et al. (2016), respectively.

Pallasite	Metal (vol.%)	Pyroxene		Olivine	Chromite*	
		Opx	Cpx		$Fe^{\#}$	$Al^{\#}$
Zinder	43	$Wo_{2.0}En_{86.6}Fs_{11.4}$	$Wo_{39.3}En_{55.2}Fs_{5.5}$	$Fa_{11.9}$	51.4–77.6	12.5–31.4
NWA 1911	24.3	$Wo_{1.6–1.8}En_{86.5–87.0}$(core) $Wo_{1.9–2.3}En_{86.3–86.6}$ (rim)	$Wo_{41.2–46.8}En_{53.5–49.2}$	$Fa_{10.8–12.3}$	44.6–66.0	13.9–18.6
Vermillion	86	$Wo_{1.7}En_{87.6}$	$Wo_{44.2}$–$En_{51.0}$	$Fa_{11.1–12.1}$	~60	~6
Choteau		$Wo_{1.0–3.0}En_{86.2–89.3}$	$Wo_{30.4–43.6}En_{52.2–63.2}$	$Fa_{8.5–12.6}$	52.9–64.2	11.4–17.1
NWA 10019	32.7–33.7	$Wo_{0.2–7.2}En_{77.4–85.0}$	$Wo_{44.3–48.9}En_{45.9–48.0}$	$Fa_{15.7–17.2}$	49.1–51.0, 61.5–74.1	58.8–59.3, 27.7–44.2

* Fe# = 100 × Fe/(Fe + Mg) (molar), Al# = 100 × Al/(Cr + Al) (molar). Chromite in Vermillion exists in symplectic intergrowths with Cpx and can only be estimated due to its small size.

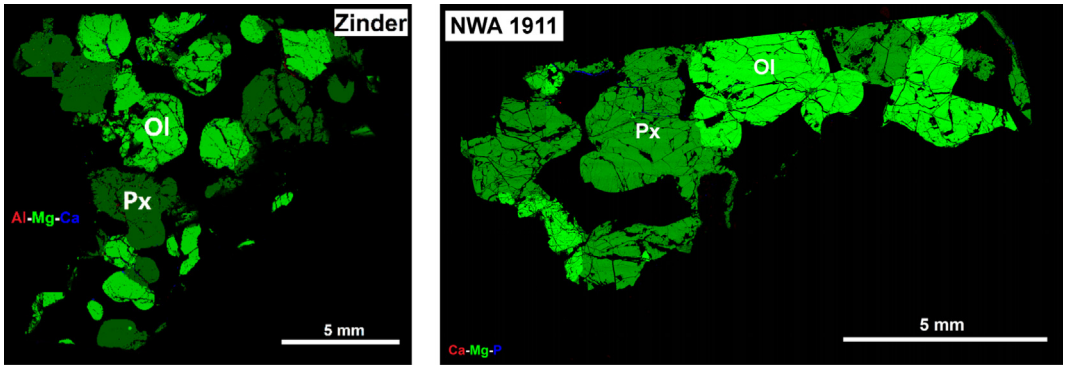

Fig. 2. Three-element X-ray map overlays for Zinder and NWA 1911 thin sections. Px = pyroxene, Ol = olivine. (For interpretation of the colors in the figure, the reader is referred to the web version of this article.)

Quantitative analysis was performed with three separate calibrations: one for olivine and pyroxene, a second for chromite and phosphate, and a third for metal, phosphide, and sulfide. Operating conditions of the instrument consisted of 15 kV voltage, 20 nA current, and a point beam for all three calibrations. Counting times were 45 s for on-peak, and 22.5 s for backgrounds for all elements except Na (when analyzed), which had an on-peak time of 30 s. The data were calculated using PAP correction procedures (Pouchou and Pichoir, 1991). One-sigma standard deviations are <1% for major elements and 3–8% for minor elements. Element mapping was performed at a resolution of 5 micrometers per pixel for NWA 1911 and 6 micrometers per pixel for Zinder with dwell times of 0.015 s for both meteorites. Silicon, Al, Cr, Fe, Mg, Ca, Na, P, and Ni maps were generated for both Zinder and NWA 1911 along with backscattered electron (BSE) maps. The analytical spots and lines of Zinder and NWA 1911 are shown in Appendix 4, EMPA standard details in Appendix 5, and detailed EMPA data of Zinder in Appendix 6 and NWA 1911 in Appendix 7.

A summary of mineralogical compositions of Zinder, NWA 1911, and other pyroxene-bearing pallasites is shown in Table 4. Zinder is a pyroxene pallasite (cf. Boesenberg et al., 2000) and consists of ~43 vol.% Fe-Ni metal (kamacite and trace taenite) and 55 vol.% silicate with olivine

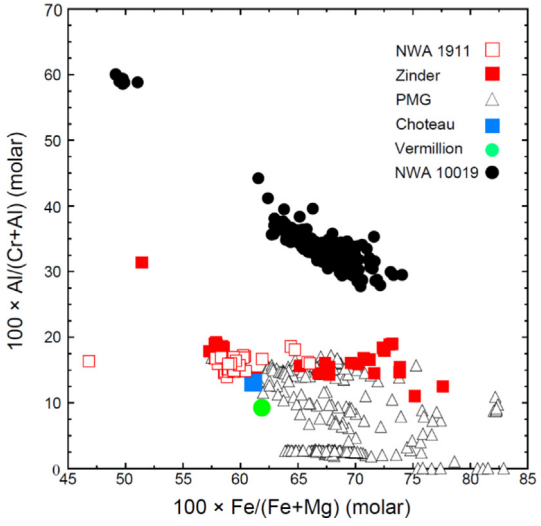

Fig. 3. Fe/(Fe + Mg) versus Al/(Al + Cr) plot showing chromite from NWA 1911, Zinder, other pyroxene pallasites (Choteau, Vermillion, and NWA 10019), and the PMG. The data of Choteau, Vermillion, and NWA 10019 are from Gregory et al. (2016), Boesenberg et al. (2000), and Boesenberg et al. (2016), respectively. (For interpretation of the colors in the figure, the reader is referred to the web version of this article.)

and orthopyroxene present in near-equal proportions (Fig. 2). Trace amounts of clinopyroxene, chromite, merrillite, troilite, and schreibersite are present. Fine-grained inclusion assemblages of chromite + troilite + merrillite ± metal are scattered inside the large olivine and orthopyroxene grains. Orthopyroxene + troilite or chromite + clinopyroxene symplectites also occur. Olivine and orthopyroxene are composed of rounded, 1–2 mm grains, and some small fragments. Both olivine and orthopyroxene are present as rare inclusions in the other phases. The large olivine ($Fa_{11.9}$, Fe/Mn = 33.6) and orthopyroxene ($Wo_{2.0}En_{86.6}Fs_{11.4}$, Fe/Mn = 20.6) grains show no chemical variations between different grains and are thus equilibrated. The inclusions, however, have slightly different compositions, with the olivine being more FeO-rich ($Fa_{12.7}$, Fe/Mn = 34.7) and the orthopyroxene being more MgO-rich ($Wo_{1.0}En_{87.7}Fs_{11.3}$, Fe/Mn = 11.3) than the larger grains. Clinopyroxene is present as both a 100 × 20-μm-long rim along an olivine grain ($Wo_{39.3}En_{55.2}Fs_{5.5}$, Fe/Mn = 17.5) and as 20–50 μm rounded inclusions ($Wo_{45.6–47.8}En_{48.1–49.5}Fs_{4.0–6.3}$, Fe/Mn = 7.5–11.6) in both olivine and orthopyroxene. Chromite is present in different textural settings: as a large grain, small inclusions within olivine and orthopyroxene, and in fine-grained symplectites. The compositions vary (100 × Fe/(Fe + Mg) = 51.4–77.6, 100 × Al/(Cr + Al) = 12.5–31.4) and are similar to the most Al_2O_3-rich chromite grains found in the main-group pallasites (PMG) (Fig. 3). Merrillite is the only phosphate present.

NWA 1911 is another pyroxene pallasite, very similar to Zinder; it has modal mineralogical abundances (vol.%) of olivine 40.2%, orthopyroxene 34.5%, metallic Fe-Ni 24.3%, and troilite and chromite 1% (Bunch et al., 2005). A trace amount of merrillite was also identified in this study. The olivine [($Fa_{10.8–12.3}$, mean = 11.9), Fe/Mn = 35.6 (N = 56, 6 grains)] in NWA 1911 is rounded to sub-angular and generally 2–4 mm in diameter. Pyroxene occurs in a variety of settings and is present both as orthopyroxene and clinopyroxene. The orthopyroxene occurs as (1) rounded, up to 4-mm-diameter grains, (2) a 100-μm rounded inclusion within an olivine grain, and (3) as small (<20 μm), irregular clinopyroxene and orthopyroxene inclusions within multiple symplectites that also include troilite. The compositions of the large orthopyroxene grains vary mildly from grain to grain, primarily in CaO content, ranging from 0.85 to 1.3 wt.% CaO. The three measured large orthopyroxene grains have core compositions with a range of $Wo_{1.6–1.8}En_{86.5–87.0}$, while rims are $Wo_{1.9–2.3}En_{86.3–86.6}$. All three grains have approximately equal concentrations of TiO_2 (~0.13 wt.%), Al_2O_3 (~0.95 wt.%), and Cr_2O_3 (~0.85 wt.%), and similar Fe/Mn ratios of 20–23. The 100-μm orthopyroxene inclusion found in olivine contains similar TiO_2, Al_2O_3, and Fe/Mn ratios as the large grains, but lower Cr_2O_3 (~0.63 wt.%). The clinopyroxene occurs only as 10 μm or smaller inclusions in the symplectites with a compositional range of $Wo_{41.2–46.8}En_{53.5–49.2}$ and Fe/Mn = 18.3 (N = 8, 8 grains) with low Cr_2O_3 (~0.28 wt.%) and TiO_2 (~0.15 wt.%). Chromite is present both as small grains (tens of micrometers in diameter) and large grains (hundreds of micrometers in diameter) between and adjacent to olivine and metallic Fe-Ni; some chromite grains contain merrillite inclusions. Chromite also occurs in the fine-grained symplectites along with troilite, clinopyroxene, orthopyroxene, and olivine. The chromite compositions (100 × Fe/(Fe + Mg) = 44.6 to 66.0, 100 × Al/(Cr + Al) = 13.9 to 18.6) are similar to the most Al_2O_3-rich chromite grains found in the PMG (Fig. 3) and overlap those in Zinder (although they cover a larger Fe/(Fe + Mg) range). Merrillite is the only phosphate present. Troilite is uncommon and can be found in multiple symplectite (troilite + orthopyroxene + clinopyroxene ± olivine ± chromite) regions. Olivine compositions that border symplectite regions are slightly more MgO-rich (Fa ~11) than other regions.

The chromite and merrillite compositions of Zinder and NWA 1911 are richer in Al_2O_3 and Na_2O than those of PMG, but are otherwise similar. Nevertheless, pyroxene-bearing pallasites are more complex than other pallasites (Boesenberg et al., 2000). The presence of two pyroxenes within Zinder indicates this meteorite likely formed on a parent body with a lower degree of partial melting than the PMG (Sunshine et al., 2007). The pyroxene also indicates a radically different bulk silicate composition in the respective parts of the core/mantle in which these meteorite samples crystallized. The differences between the various pyroxene pallasites (Vermillion, Yamato 8451, NWA 10019, Choteau, Zinder, NWA 1911) are more marked than their similarities, particularly with respect to metal composition. In contrast to other pyroxene pallasites, Zinder has metal with high Ir and significant depletions in volatile elements. High abundances of refractory, compatible elements also occur in the Eagle Station pallasites, although O-isotopic compositions indicate no close relationship between the Eagle Station group and Zinder (Bunch et al., 2005).

In summary, NWA 1911 and Zinder are nearly identical in their major, minor, and mineral compositions (Tables 3 and 4). All mineral-composition ranges overlap, including olivine, orthopyroxene, clinopyroxene, chromite, merrillite and metallic Fe-Ni. Some phases, such as chromite, have a larger range in one meteorite or the other, but that may be attributable to non-representative sampling.

3. FRACTIONAL-CRYSTALLIZATION MODELING

3.1. Modeling methods

A simple fractional-crystallization model method (without the consideration of trapped melt) is described in Chabot (2004), and a trapped-melt model method is detailed in Chabot and Zhang (2021). Both fractional-crystallization models calculate batch equilibrium crystallization in small steps to model fractional crystallization with values for the partition coefficients that change as the liquid composition changes during crystallization. In particular, the S and P contents are known to have a substantial influence on the solid metal/liquid metal partition coefficients of siderophile elements in the Fe-Ni-S-P system that are relevant to the crystallization of iron meteorites (e.g., Chabot et al., 2017), and we include those effects in

our models. This fractional-crystallization approach assumes a well-mixed core in which solid metal crystallizes in small steps and is efficiently removed and isolated from the liquid after each step. The remaining liquid, acting as an initial composition, repeats this fractional crystallization for another step, and so on. Previous modeling studies of the IIIAB core (Wasson, 1999, 2003, 2016) and the IIAB core (Wasson et al., 2007) invoked trapped pockets of metallic melt during fractional crystallization, with some IIIAB and IIAB irons forming as products of equilibrium mixing between solid and liquid. In the revised trapped-melt model (Chabot and Zhang, 2021), the metallic portion of the irons is envisioned to have resulted from mixing of the solid metal from fractional crystallization and the solid metal that crystallized from the trapped melt. The revised trapped-melt model includes the influence on the element concentrations due to the formation of troilite from the trapped melt. More details of the modeling methods described above are included in Appendix 8.

In the following text, "simple fractional-crystallization model" means simple fractional crystallization of a metallic melt without consideration of trapped melt; "trapped melt model" means that the influence of the formation of trapped melt is considered; "fractional crystallization" may refer to either model.

3.2. Modeling results

We began our modeling efforts by considering the simplest model: a S-only model without trapped melt. While both S and P can affect the solid metal/liquid metal partition coefficients (e.g., Chabot et al., 2017), the amount of S that has been modeled to be present in the parent-body cores of magmatic iron meteorites varies considerably, from 0 wt.% to 17 wt.% (Wasson, 1999; Wasson and Richardson, 2001; Chabot, 2004; Campbell and Humayun, 2005; Wasson and Huber, 2006; Wasson et al., 2007; Walker et al., 2008; Hilton et al., 2020; Tornabene et al., 2020). Furthermore, measurements of the metallic phases of iron meteorites do not provide any constraint on the amount of S that might have been present during crystallization because S does not partition into the crystallizing Fe-Ni metal at the conditions under which iron meteorites solidified (Massalski and Subramanian, 1990). Thus, to model

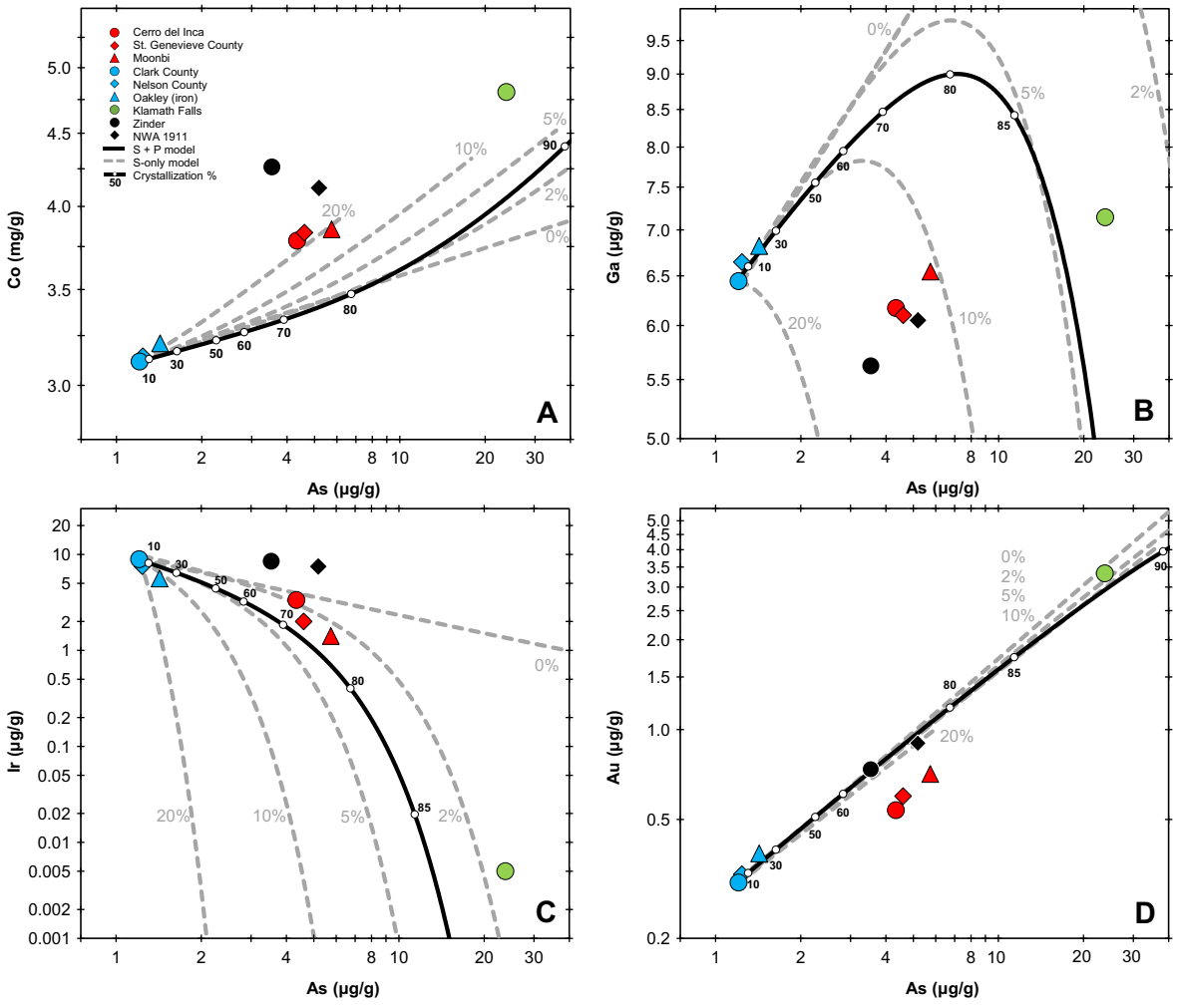

Fig. 4. S-only model (dashed lines; various initial wt.% S) and S + P model (solid black lines; initial 2.0 wt.% S and 1.3 wt.% P) for Co, Ga, Ir, and Au vs. As plots. (For interpretation of the colors in the figure, the reader is referred to the web version of this article.)

the fractional crystallization of a magmatic iron-meteorite group, it is important to examine a range of different initial S compositions.

Our model is based on the assumption that the lowest-As irons were the first solids to crystallize in the IIIF core. We tested various initial S contents (0 wt.%, 2 wt.%, 5 wt.%, 10 wt.%, 20 wt.%) to narrow down the range of S contents that best fit the Co, Ga, Ir, and Au vs. As plots (Fig. 4). Cobalt, Ga, Ir and Au are chosen here because they have distinct crystallization behaviors, with partition coefficients that are influenced by the presence of S to differing levels (Chabot et al., 2017); thus, examining elements with a range of behaviors as a function of the S content of the liquid can provide multiple constraints to best evaluate the S content of a parent body core (e.g., Chabot, 2004; Chabot and Zhang, 2021; Wasson, 1999; Wasson and Richardson, 2001). The elements were plotted against As instead of Au because (1) Au and As have almost the same partition coefficients in the Fe-Ni-S-P system (e.g., Chabot et al., 2017), (2) As can also be determined by INAA with high precision (see Section 2.1) and (3) the chemical behavior of Au is more poorly understood in low-S metallic melts than that of As (Chabot et al., 2017). Wasson (1999) suggested that either Au or As was a good choice against which to plot elemental trends in magmatic iron meteorites.

Fig. 4 shows that all S contents do not fit these four element-As trends at the same time. Cobalt and Ga are a notable issue as none of the S contents can fully account for their trends. The Ir-As trend can be reasonably fitted using 2 wt.% S. The initial S contents of 0–10 wt.% work for the Au-As trend, except that Moonbi, St. Genevieve County, and Cerro del Inca deviate from the model trends. Despite the poor fitting of Co and Ga, we prefer 2–5 wt.% S for further modeling of other elements, because the range works somewhat better than other S contents (if Klamath Falls is included).

We next added the effect of P to the model, using the P vs. As diagram (Fig. 5A) to constrain the initial P content to a value of 1.3 wt.%. Modeling the crystallization trend of P in iron meteorites is known to be complicated due to the formation of schreibersite subsequent to crystallization of the metal (Chabot and Zhang, 2021). It seems likely that the amount of P now present in IIIF metal is lower than the amount that was present in the metal during initial crystallization, prior to the sub-solidus formation of schreibersite (which removed P and Ni from the metal phase). Thus, modeling P content of the initial liquid by fitting the current-day IIIF P values of the solid metal is a lower limit of the actual P content present during fractional crystallization.

After setting the P content at 1.3 wt.%, a trial-and-error method was used for the S + P model to find a S content (within the range of 2–5 wt.%) that produced the best fits to as many elements as possible. As a result, the S + P model with initial concentrations of 2.0 wt.% S and 1.3 wt.% P was selected. The S + P model was used to model 19 element-As trends of the IIIF irons (Fig. 5). The figure also includes the results from the application of the revised trapped melt model (Chabot and Zhang, 2021), showing how elemental concentrations change in the fractionally crystallized metal, liquid, and trapped-melt metal. The mixing curves of metals from fractional crystallization and trapped melt are shown at 10%, 50% and 80% crystallization. Chromium was not included in the modeling because it is known to occur in accessory minerals such as chromite as well as in metallic iron (Wasson and Richardson, 2001). Vanadium and Mn were not included in the modeling because parameterizations of their partitioning behaviors are incomplete or absent for the Fe-Ni-S-P system (Chabot et al., 2017). It should be noted that the influence of the formation of minor phases on Ni, Cu, and Mo contents is not considered in this study. Nickel and Mo are known to partition into schreibersite and Cu into troilite, which can affect the metallic composition of the remaining Fe-Ni. These elements may preferentially partition into schreibersite or troilite so that their concentrations in metal do not follow fractional-crystallization trends (Chabot and Zhang, 2021). Other siderophile elements are more suitable for constraining the fractional-crystallization model as their concentrations are not significantly affected by the occurrence of schreibersite or troilite. The initial concentrations of elements used in the model is shown in Appendix 9.

4. DISCUSSION

4.1. Fractional-crystallization modeling

The S + P fractional-crystallization model shown in Fig. 5 produces trends that are generally consistent with those of the HSEs: Ru, Re, Os, Ir, Pt, and Au. The Mo concentrations of IIIF irons shown in Fig. 5F are very scattered and do not suggest a fractional-crystallization trend. Similarly, scatter in the trends or discrepancy with the fractional-crystallization model in Fig. 5D for Cu may be due to its chalcophile nature (Chabot et al., 2017). The Co variation observed in IIIF irons is wider than what the model predicts (Fig. 5B), and the Pd variation is less than what the model predicts (Fig. 5J). The trends for both Sn (Fig. 5K) and Sb (Fig. 5L) have members that do not define a clear trend and hence cannot all be fitted by a single fractional-crystallization model. The Rh data (Fig. 5I) similarly do not appear to define a clear single trend among all members of the group.

Additionally, the IIIF trends for both Ga (Fig. 5E) and Ge (Fig. 5G) are not matched by the fractional-crystallization model. This inconsistency between the model predictions and the meteorite analyses for Ga and Ge is notable because the classification of group IIIF is based on their similar Ga and Ge abundances. During the fractional crystallization of a metallic core, a typical Ga- or Ge-Au/As trend is part of a parabola opening downward because the compatibility of Ga and Ge changes (incompatible to compatible) as the S content in the liquid increases (Chabot et al., 2017), as shown in Fig. 4B. The Ga- and Ge-As trends of IIIF irons either show minimal variation in their Ga and Ge contents, or they resemble a parabola opening upwards; neither is consistent with the fractional-crystallization trends produced by any S content (Fig. 4B). Thus, the Ga and Ge concentrations in IIIF irons cannot be fitted by the fractional-crystallization model.

A recent study used ICP-MS data and performed fractional-crystallization modeling of HSEs, Re, Os, Ir, Ru, Pt, Pd, in group IIIF (Hilton et al., 2021). Their modeling method is essentially the same as ours. Their HSE data can be best fit using 5 wt.% S and 1 wt.% P. In their model, most of the IIIF irons stay on the solid tracks, while

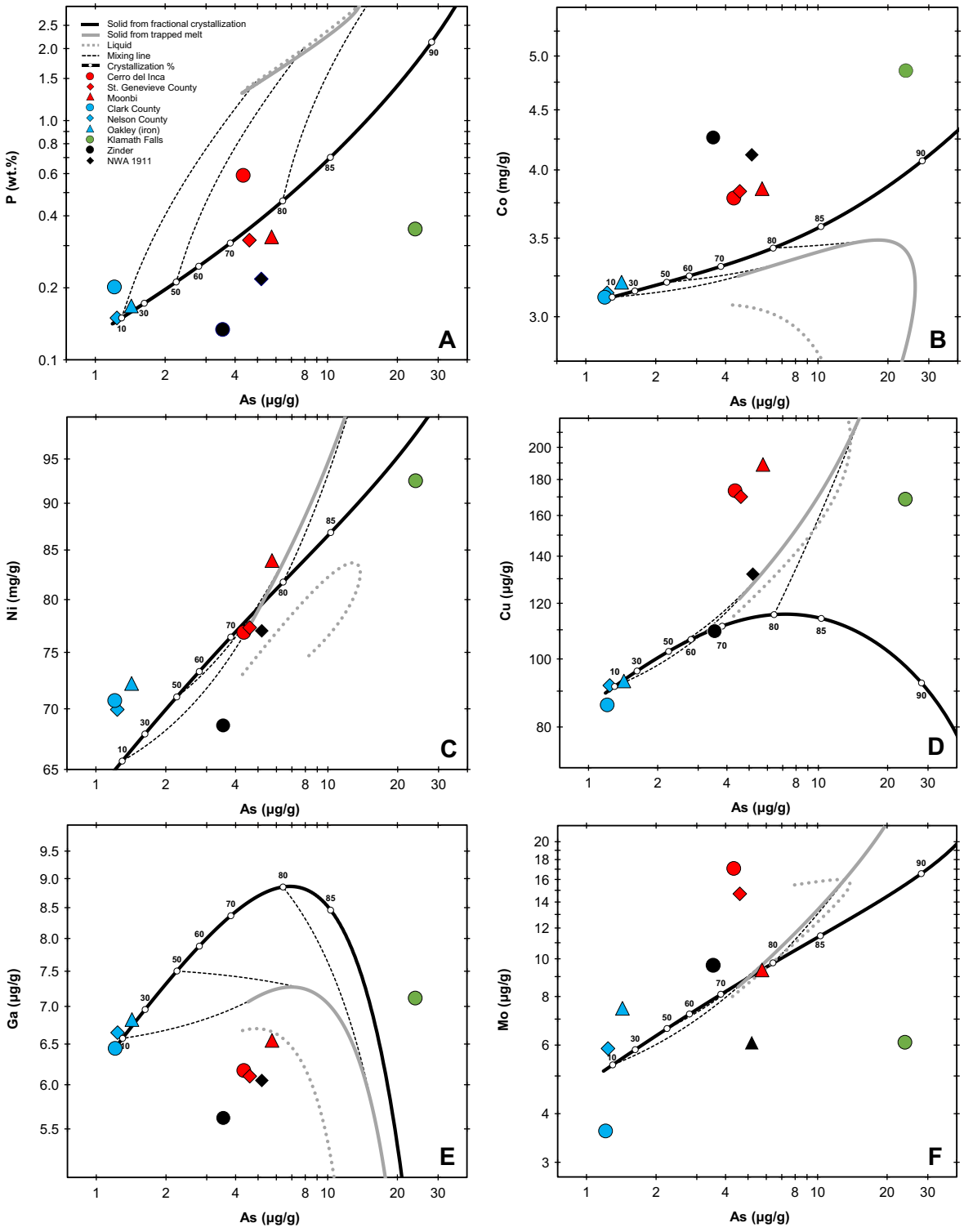

Fig. 5. S + P fractional-crystallization modeling of IIIF irons. The black solid lines are the solid tracks from simple fractional crystallization; dotted lines are liquid tracks; gray lines are the solid formed from trapped melt; dashed lines denote the mixing lines of the two solid tracks at 20%, 50% and 80% crystallization of the core. Nickel, P, Cu, and Mo concentrations may be affected by the occurrence of accessory phases (see Section 3.2). (For interpretation of the colors in the figure, the reader is referred to the web version of this article).

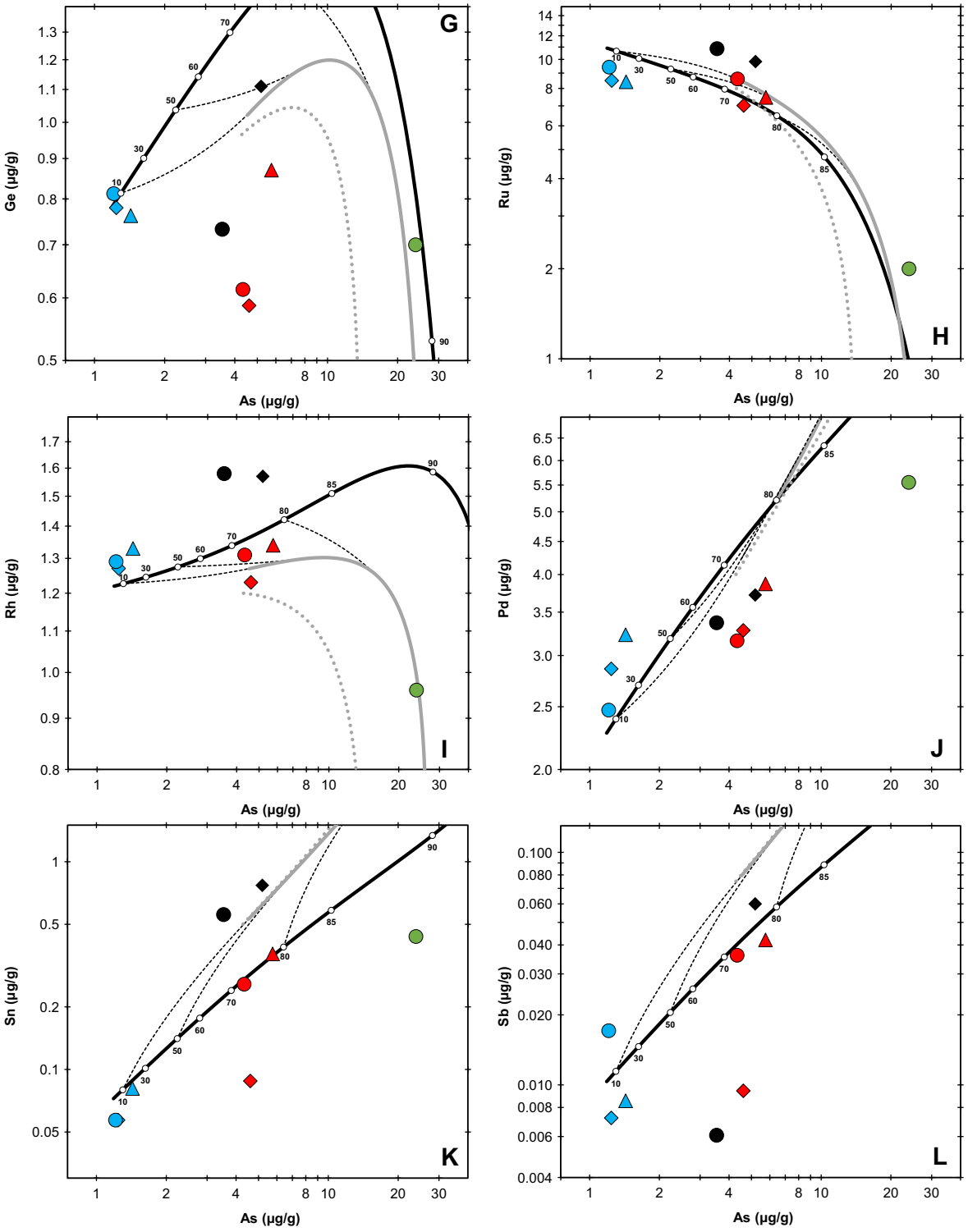

Fig 5. *(continued)*

Klamath Falls deviates slightly from the solid tracks. Likewise, our modeling shows that HSE vs. As trends are generally consistent with the model tracks using a starting composition of 2 wt.% S and 1 wt.% P. However, some crucial elements, such as Co and Ga, that group IIIF was based on initially, cannot be fitted using either 2 wt.% or 5 wt.% S (Fig. 4). The HSE model of Hilton et al. (2021) does not take the constraints from Co and Ga into account,

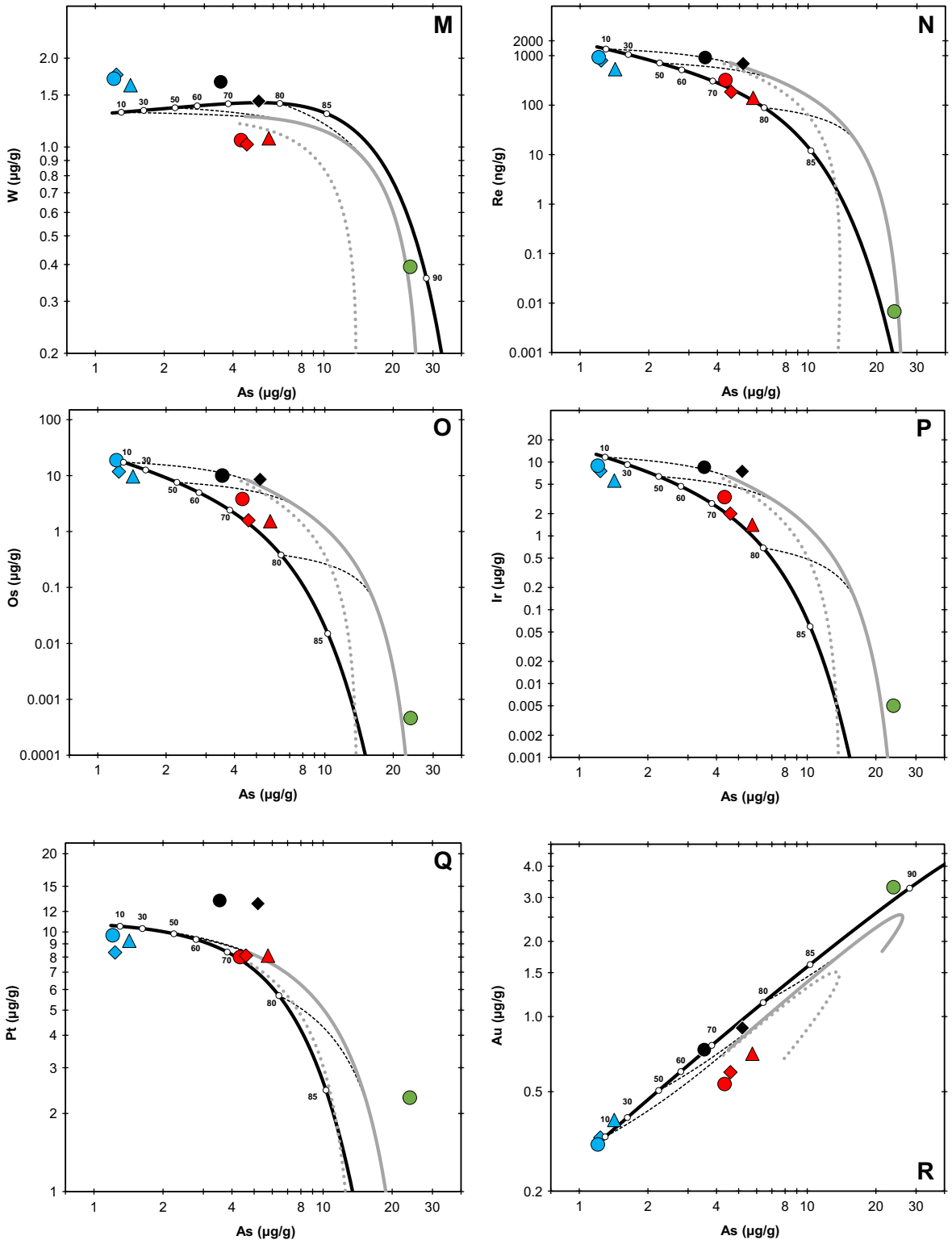

Fig 5. *(continued)*

and applying the Hilton et al. (2021) model to elements beyond the HSEs does not produce elemental trends that can match these full IIIF compositions.

In brief, the IIIF trends for all the elements examined in this study cannot be fitted by a single fractional-crystallization model, and in particular, the IIIF Co, Ga

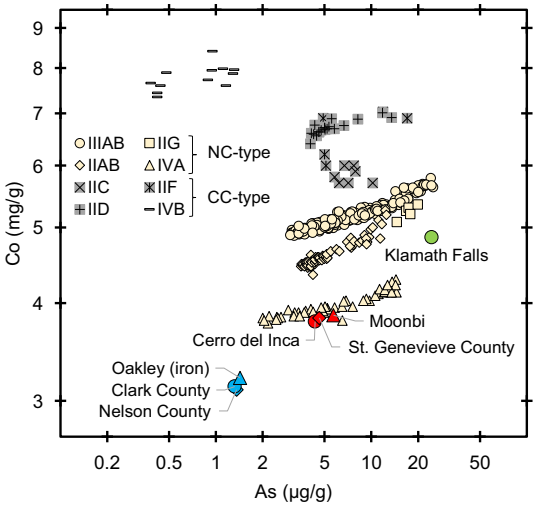

Fig. 6. Co-As trends of magmatic iron groups. A: Gray symbols denote CC-type iron groups, and beige symbols denote NC-type iron groups. Group IIG has not been classified as CC or NC classification by stable isotopic studies, but is assumed to be NC-type due to its genetic relationship with group IIAB (Wasson and Choe, 2009). Group IIIF is shown in yellow, blue, red, and green symbols. Data of IIAB, IIC, IID, IIF, IIG, IIIAB, IVA, and IVB are from Wasson et al. (2007), Tornabene et al. (2020), Wasson and Huber (2006), Hilton et al. (2020), Wasson and Choe (2009), Chabot and Zhang (2021), Wasson and Richardson (2001), and Campbell and Humayun (2005), respectively. (For interpretation of the colors in the figure, the reader is referred to the web version of this article).

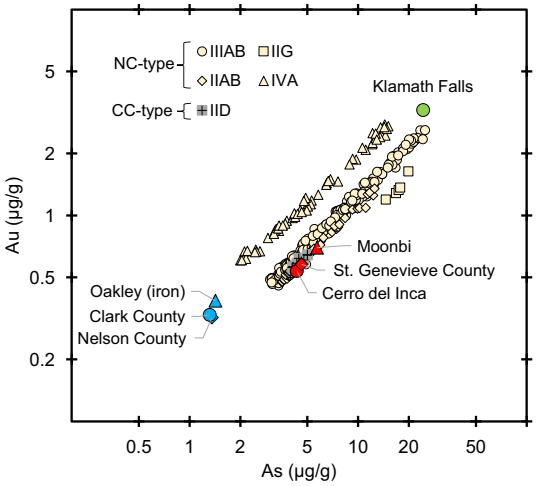

Fig. 7. Au-As trends of selective magmatic iron groups. Gray symbols denote CC irons; beige symbols denote NC irons. The NC and CC classification is based on Kruijer et al. (2017). Group IIIF is marked by red, blue and green symbols. Group IIG is assumed to be NC-type due to its genetic relationship with group IIAB (Wasson and Choe, 2009). Data of IIAB, IIG, IIIAB, IVA, IID are from Wasson et al. (2007), Wasson and Choe (2009), Chabot and Zhang (2021), Wasson and Richardson (2001), and Wasson and Huber (2006), respectively. Only INAA data are plotted here because ICP-MS data in the literature usually have relatively large analytical errors (sometimes >10%) for Au and As, which may induce Au-As displacements, and a consistent dataset is needed to distinguish the subtle trend differences shown in this Au-As plot. (For interpretation of the colors in the figure, the reader is referred to the web version of this article.)

and Ge trends are not consistent with those expected from fractional crystallization. Thus, group IIIF behaves differently than many other magmatic groups, e.g., IIAB (Chabot, 2004), IID (Wasson and Huber, 2006), IIIAB (Chabot and Zhang, 2021) and IVB (Campbell and Humayun, 2005). This conclusion led us to consider the crystallization of group IIIF in more detail, as discussed in the next four sections.

4.2. The Co vs. As trend

The range of Co concentrations in IIIF irons is the widest among those in all magmatic iron-meteorite groups (Fig. 6). Cobalt concentrations in a magmatic group typically exhibit minimal variation as the metal/liquid partition coefficient for Co stays near unity over the course of fractional crystallization of metallic melts (Chabot et al., 2017). The steep slope of the IIIF Co vs. As trend is also exceptional among magmatic iron groups (Fig. 6). Such a steep slope may be produced by high initial S contents, such as ~20 wt.% S as shown in Fig. 4A, but in this case, the Fe-FeS eutectic composition would be reached significantly before the formation of Klamath Falls. Additionally, such a high initial S content of 20 wt.% would be completely inconsistent with the IIIF Ir vs. As trend (Fig. 4C). The wide variation of Co for IIIF irons do not conform to fractional crystallization.

4.3. The Au vs. As trend

The three irons Moonbi, St. Genevieve County, and Cerro del Inca (which we refer to as the Moonbi grouplet) are displaced from other IIIF irons on the Au-As diagram (Fig. 5R). Gold and As have almost identical chemical behaviors during the fractional crystallization of metallic melts (Chabot et al., 2017); thus, the Au-As trend is typically linear for a magmatic iron group. The position of a magmatic group on the Au-As trend is determined mainly by the initial Au/As ratio of the group's parent melt. We compiled the Au-As trends of five magmatic iron groups together with group IIIF in Fig. 7. It shows that the Moonbi grouplet does not fall on the Au-As trend formed by the other IIIF irons, but it does fall on the trends of other major magmatic iron groups.

Such Au-As displacement within a single group has not been found previously (Fig. 7) (Wasson et al., 2007; Wasson and Choe, 2009; Chabot and Zhang, 2021; Wasson and Richardson, 2001; Wasson and Huber, 2006) (although it was reported between the genetically related groups IIAB and IIG; Wasson and Choe, 2009). Groups IIAB and IIG may have originated in the same asteroid, wherein IIAB irons were from a magma richer in S and IIG irons were from a related P-rich magma (as signified by their very high schreibersite contents: 11–14 wt.%) (Wasson and Choe,

2009). The Au-As offset between the IIAB and IIG groups shown in Fig. 7 was likely caused by the high As contents in IIG irons potentially due to the diffusion of As (a congener of P) from schreibersite to metal at lower temperatures (Wasson and Choe, 2009). Unlike group IIG, the Moonbi grouplet has very low contents of schreibersite (modal P = 0.18–0.28 wt.%) (Table 1), so the Au-As displacement of the Moonbi grouplet irons is unlikely to have been caused by As transferred from schreibersite into metal. If the IIIF irons constitute a coherent group and all hail from the same parent body, the As-Au displacement implies that the crystallization of IIIF irons probably involves more complicated processes in addition to fractional crystallization.

4.4. Structural variation among IIIF irons

Wasson and Kimberlin (1967) stated the possession of "similar structures" is one of the key criteria needed to define an iron-meteorite group. Before the chemical classification of irons was proposed (Goldberg et al., 1951), Widmanstätten patterns (kamacite bandwidths) were used to classify iron meteorites (e.g., Scott, 2020). Most iron-meteorite groups have a relatively narrow range of structural types (e.g., Lovering et al., 1957; Scott, 2020; Wasson and Kimberlin, 1967. Table 5 summarizes the structural classes and kamacite bandwidths of magmatic iron groups (Buchwald, 1975). There are eight structural classes and some iron groups share the same structural classes. For example, groups IID and IIAB are both dominated by medium octahedrites, whereas group IVB is the only magmatic group whose members are all ataxites. According to Table 5 summerized from Buchwald (1975), a single iron group typically has a primary structural class that comprises >80% of the members (except for group IC) and exhibits only small variations in kamacite bandwidth (coefficient of variation ≤0.20). The structural similarity applies both to groups with hundreds of members (e.g., IIIAB) and groups with few members (e.g., IIF). In contrast to other groups, group IIIF has four structural classes and only three out of seven members (43%) have the primary octahedrite structure (Fig. 8). The coefficient of variation of the kamacite bandwidths of group IIIF is 0.47, more than twice as high as those of other groups. Group IIIF has the greatest variety of structural classes and kamacite bandwidths among all established magmatic iron groups; the structural variation makes the group deviate from the criterion that a coherent iron-meteorite group should have similar structures (Wasson and Kimberlin, 1967). The striking structural variation and the discrepancy between fractional-crystallization tracks and analytical data differentiate group IIIF from other magmatic groups.

4.5. Group IIIF: Not a simply fractionally crystallized group

We now examine if, by excluding certain members from group IIIF, the remaining members would be consistent with belonging to a fractionally crystallized core. In particular, based on the Au-As displacement of the Moonbi grouplet (Section 4.3) and the grouplet's Ga and Ge contents (Section 4.1), we exclude the Moonbi grouplet from IIIF in this exercise to test fractional-crystallization modeling on the remaining IIIF members. The exclusion of the Moonbi grouplet would leave four meteorites within group

Table 5
Structural and kamacite-bandwidth statistics of primary magmatic iron groups.

Group	Total records*	Number of structural class†	Primary class†	Fraction with primary class†	Kamacite bandwidth (mm)		
					Average	Standard deviation	Coefficient of variation**
IIC	8	1	Opl	100% (N = 6)	N/A	N/A	N/A
IID	26	2	Om	92% (N = 22)	0.72 (N = 20)	0.15	0.20
IIF	7	2	Opl	83% (N = 6)	N/A	N/A	N/A
IIIF‡	9	4	Of or Om§	43% (N = 7)	0.74 (N = 6)	0.35	0.47
IVB	18	1	D	100% (N = 17)	N/A	N/A	N/A
IC¶	13	3	Og	50% (N = 10)	2.47 (N = 3)	0.48	0.19
IIAB + IIG#	141 + 6	2	H	83% (N = 18)	N/A	N/A	N/A
IIIAB	321	1	Om	100% (N = 30)	1.04 (N = 30)	0.21	0.20
IIIE	18	2	Og	90% (N = 10)	1.44 (N = 10)	0.10	0.07
IVA	81	1	Of	100% (N = 23)	0.32 (N = 23)	0.05	0.14

* Total records of these groups are from the Meteoritical Bulletin Database. The anomalous irons of a group are not included.
† Information and data from Buchwald (1975). Data of large Groups IIAB and IIIAB only used those recorded in Buchwald (1975) to ensure consistent measurements and petrographical observations. "N" equals the total number of irons recorded in Buchwald (1975), as it does also in the Average column. D = ataxite, Opl = plessitic octahedrite, Of = fine octahedrite, Om = medium octahedrite, Og = coarse octahedrite, H = hexahedrite.
‡ Only seven IIIF (here excluding Fitzwater Pass and Binya) recorded in the Meteoritical Bulletin Database are included in the statistics. See Table 1 for more information.
§ Cerro del Inca has a transitional texture between Of and Om, so it is counted as either of the two structures.
¶ The kamacite-bandwidth average and standard deviation of Group IC may not be representative because there are only data for three members available.
# Groups IIAB and IIG may be from the same parent body but different portions of the core (Wasson and Choe, 2009).
** Coefficient of variation equals to *standard deviation* divided by *average*.

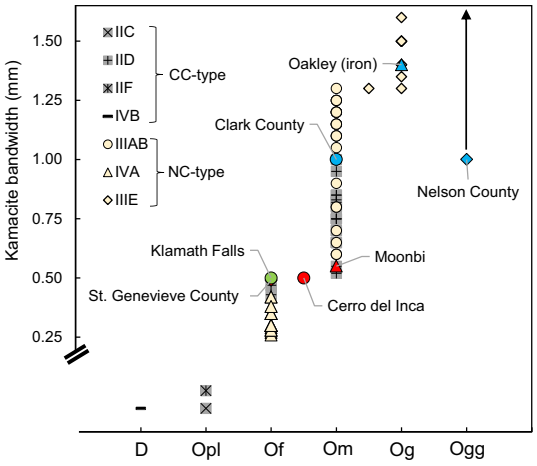

Fig. 8. Kamacite-bandwidth distribution of group IIIF compared with those of other major magmatic iron groups. All structural classes and kamacite bandwidths are from Buchwald (1975), except for those of Klamath Falls from Kracher et al. (1980) and Cerro del Inca from the Meteoritical Bulletin Database. Groups IIF, IIC and IVB are ataxites or plessitic octahedrite, so their kamacite bandwidth data are absent. The seven IIIF members shown here have four structural classes, and Nelson County has a range of bandwidth of 1–10 mm. The NC-CC classifications of magmatic iron groups from Kruijer et al. (2017). D = ataxite, Opl = plessitic octahedrite, Of = fine octahedrite, Om = medium octahedrite, Og = coarse octahedrite, Ogg = coarsest octahedrite. (For interpretation of the colors in the figure, the reader is referred to the web version of this article.)

IIIF. The range of Ir contents in such a group would still be quite large: Klamath Falls has an Ir concentration >1000 times lower than that of the four other remaining IIIF irons. If these four irons indeed originated by fractional crystallization of the same parent melt, they should represent very early (<10%) and late (>85%) crystallization products, according to the models of Figs. 4 and 5. We can test whether Klamath Falls and the Clark County grouplet (Clark County, Nelson County, Oakley (iron)) are plausible end members of a fractional-crystallization model.

We adjusted the model with a slightly lower initial S (1.2 wt.%) and higher P (1.4 wt.%) and other initial elemental concentrations to make the Clark County grouplet the starting point of crystallization. The resultant diagrams are shown in Appendix 10. The revised model works reasonably well for the Ni and Ga vs. As trends of the four remaining members and for the Ni, Ga, Ge, Ru, Os and Au vs. As trends of the Clark County grouplet and Klamath Falls, but the model still cannot account for other element-As trends. As mentioned in Section 4.2, the wide Co variation provides evidence that Klamath Falls may not be a fractional-crystallization product from the same parent melt as the Clark County grouplet.

Another scenario is to consider if the Clark County grouplet and Moonbi grouplet constitute a single fractional-crystallization sequence. On the Co- and Ga-As diagrams (Figs. 4A and 4B), the two grouplets can be fitted using 10–20 wt.% S, while on the Ir-As diagram (Fig. 4 C), they can be fitted with 0–5 wt.% S. The Au-As trend of the Clark County grouplet and Moonbi grouplet cannot be fitted using any S contents (Fig. 4D). It seems that, as in the previous models, the two grouplets cannot be fitted for the four key interelement trends using a single S content. The fractional-crystallization models of the truncated group IIIF further demonstrate that fractional crystallization alone cannot explain the interelement trends of group IIIF.

The classification of group IIIF irons was made originally on the basis of the narrow range of Ni, Ga, and Ge contents, unusually high Ga/Ge ratios, low Co contents, and IIIAB-like or steeper chemical trends for many elements (Scott and Wasson, 1976; Kracher et al., 1980). The background density of ungrouped irons in Ni-Ga-Ge space in the IIIF region is very low (Scott and Wasson, 1976), which could be evidence that it is unlikely that the IIIF members are unrelated irons that happen to have similar chemical compositions. It also seems unlikely that seven ungrouped irons would define IIIAB-like chemical trends on interelement plots. Our fractional-crystallization modeling relies on the assumption that a magmatic iron core fractionally crystallized from a homogeneous melt that has vigorous convection, during which no significant secondary processes (e.g., impact disruption, substantial dendrite growth, non-equilibrium mixing of liquids and solids, etc.) occurred. Therefore, although group IIIF displays elemental trends that are not well matched by a fractional-crystallization model and wide structural variations that are distinct from any other magmatic groups, it is possible that the IIIF irons may have crystallized from a single metallic melt with additional secondary processes involved. If so, group IIIF would provide a unique opportunity to investigate iron-meteorite crystallization under more complex conditions.

However, more isotopic data are needed to provide tighter constraints on the origin and genetic relationships of IIIF irons. Currently, the CC classification of group IIIF is primarily based on Oakley (iron), Clark County, and Klamath Falls, and their Mo and Ru isotopes point towards a CC origin (Kruijer et al., 2017, 2019; Worsham et al., 2019). Nitrogen isotopes of Nelson County support the CC classification of group IIIF (Prombo and Clayton, 1993; Grewal et al., 2021). Klamath Falls deviates slightly from other magmatic groups in the $^{187}Re/^{188}Os$ vs. $^{187}Os/^{188}Os$ isochron (Hilton et al., 2021), which could imply that the system was disturbed, although this measurement may also be complicated due to the very low concentration of HSEs in this meteorite. The Moonbi grouplet has not been analyzed for Mo, Ru, or W isotopes that would permit further evaluation of its origin. Sulfur isotopes of Moonbi and Cerro del Inca were analyzed by Antonelli et al. (2014). The two Moonbi grouplet irons have the lowest $\Delta^{33}S$ and $\Delta^{36}S$ values among all iron-meteorite groups. The S-isotopic data of the Moonbi grouplet do not provide sufficient information to distinguish its CC-NC classification or its genetic connection to other IIIF irons.

4.6. Cogenetic Zinder and NWA 1911 and their possible relationship to the Moonbi grouplet

Our petrographic observations and EMPA analyses show that Zinder and NWA 1911 are nearly identical in their major, minor, and trace-element mineral compositions (Section 2.5). The similarity carries over to their O-isotopic compositions. Zinder ($\delta^{18}O = 3.39$, 3.27 and $\delta^{17}O = 1.79$, 1.81 and $\Delta^{17}O = +0.01$, $+0.09$) and NWA 1911 ($\delta^{18}O = 3.23$, 3.42 and $\delta^{17}O = 1.51$, 1.62 and $\Delta^{17}O = -0.20$, -0.19) have essentially the same average $\delta^{18}O$ composition (Bunch et al., 2005), but slightly different $\delta^{17}O$ compositions with Zinder having higher $\Delta^{17}O$ and plotting above NWA 1911 in Fig. 9. The silicate samples measured by Bunch et al. (2005) were carefully acid washed, but we suspect that one or both meteorites have had their O-isotopic compositions affected by terrestrial contamination. NWA 1911 appears more weathered than Zinder. Even if we assume that the O-isotopic difference is resolved by subsequent measurements, a difficulty with pairing these two meteorites is that their find locations (NWA 1911: Rissani, Morocco; Zinder: Zinder, Niger) are separated by ~2400 km. Tektite strewn fields are known to be this wide (Glass, 1990), but not meteorite strewn fields. Nevertheless, the similar elemental composition of the metals of Zinder and NWA 1911 and the close O-isotopic compositions of their silicates indicate that these two pallasites likely originated on the same parent asteroid.

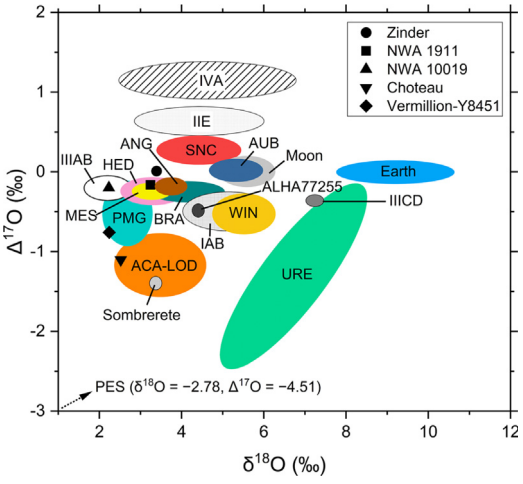

Fig. 9. Oxygen isotopes of Zinder and NWA 1911 plotted along with those of other meteorites. NWA 10019 and Vermillion-Y8541 (Vermillion and Yamato 8451) are pyroxene pallasites. Choteau is an ungrouped pallasite, possibly linked to Vermillion and Yamato 8451. Sombrerete (Worsham et al., 2017) and ALHA77255 (Spitzer et al., 2020) are CC-type ungrouped irons. Oxygen isotopes of Zinder and NWA 1911 are from Bunch et al. (2005), and those of Choteau, Vermillion-Y8541, and NWA 10019 are from Gregory et al. (2016), Boesenberg et al. (2000), Boesenberg et al. (2016); those of iron meteorites and achondrites are from Clayton and Mayeda (1996). PMG = main-group pallasites, ANG = angrites, HED = howardites, eucrites, diogenites, SNC = shergottites, nakhlites, and chassignites, AUB = aubrites, URE = ureilites, ACA-LOD = acapulcoites and lodranites, WIN = winonaites, BRA = brachinites, MES = mesosiderites, PES = Eagle Station pallasites. Groups IAB (Worsham et al., 2017), IIE (Kruijer and Kleine, 2019), IIIAB (Kruijer et al., 2017), and IIICD (Worsham et al., 2017) are NC-type. Groups IAB and IIICD are now considered as part of group IAB complex (Wasson and Kallemeyn, 2002).

The chemical compositions of the metal in Zinder and NWA 1911 are very close to those of the Moonbi grouplet (Fig. 5). Due to the low density of ungrouped irons in Ni-Ga-Ge space in the IIIF region (Scott and Wasson, 1976), the similar compositions of Zinder and NWA 1911 and the Moonbi grouplet are highly suggestive of a genetic relationship. However, the O-isotopic compositions of NWA 1911 and Zinder plot with the NC achondrites, including angrites, HEDs and SNCs (Fig. 9). We are unable to use O isotopes to confirm the relationship between these two pallasites and the Moonbi grouplet because (1) O- and Cr-isotopic data are not currently available for any IIIF irons due to the low concentrations of these elements, and (2) oxygen isotopes are less definitive for CC-NC classification. Stable isotopic data (Mo, Ru, and W) for the two pallasites and the Moonbi grouplet are needed to confirm their genetic relationship and evaluate their CC-NC affiliation. If new isotopic measurements determine that the Moonbi grouplet and the pallasites have the same CC or NC affiliation, their genetic relationship would be plausible; if such measurements show the opposite, a close relationship would be unlikely. In either scenario, an NC classification of the Moonbi grouplet would require a reevaluation of the grouping of IIIF irons.

5. SUMMARY

We report a new set of elemental data for group IIIF using both INAA and LA-ICP-MS techniques. The new data show that Fitzwater Pass should be reclassified as IAB and Binya as IIIF-an.

The fractional-crystallization modeling for the remaining IIIF irons shows that the HSE vs. As trends can be explained, but some key elements cannot. Multiple initial S contents (0 wt.%, 2 wt.%, 5 wt.%, 10 wt.%, and 20 wt.%) cannot account for the Co vs. As trend, because group IIIF has the widest Co variation among all magmatic iron groups. None of the tested initial S contents can explain the Ga-As or Ge-As trends, and notably, the IIIF classification was partially based on their similar Ga and Ge concentrations. The Moonbi grouplet (Moonbi, St. Genevieve County, and Cerro del Inca) diverges from other IIIF irons on the Au vs. As diagram.

The structural variation within the IIIF irons is striking. Group IIIF, currently with nine members according to the Meteoritical Bulletin Database, has at least four different structures, and the kamacite bandwidths of the members have a very high coefficient of variation (0.47) compared with those of other magmatic iron groups (all $\leq$0.20), while an iron-meteorite group is expected to have similar structures (Wasson and Kimberlin, 1967). The inconsistency between model tracks and some key element vs. As trends, plus the great structural variation among IIIF irons, indicate that the crystallization of IIIF irons differs from those of other magmatic iron-meteorite groups. If the IIIF

irons all formed on one parent body, the irons experienced more complex processes than straightforward fractional crystallization. Additional stable isotopic studies, of the Moonbi grouplet in particular, are needed to unveil the crystallization history and origin of group IIIF.

Two ungrouped pyroxene-bearing pallasites, Zinder and NWA 1911, have almost identical petrographic characteristics and chemical compositions (major, minor, and mineral compositions). They are clearly related to each other. The elemental compositions of metals from Zinder and NWA 1911 are close to those of the Moonbi grouplet. It is possible that the two pallasites and the Moonbi grouplet share the same parent body. The O-isotopic compositions of Zinder and NWA 1911 point to a NC-type parent body (Bunch et al., 2005; Humayun et al., 2018), but future isotopic measurements of the pallasites are necessary to constrain their CC-NC affiliation and their genetic relationship to the Moonbi grouplet.

Declaration of Competing Interest

The authors declare that they have no known competing financial interests or personal relationships that could have appeared to influence the work reported in this paper.

ACKNOWLEDGEMENTS

This manuscript is dedicated to the memory of John T. Wasson for his work over the past five decades collecting NAA data on iron meteorites. We thank the National Museum of Natural History (Smithsonian Institution) and the American Museum of Natural History for providing polished sections or metal of IIIF irons for the LA-ICP-MS analyses. We thank the Cascadia Meteorite Laboratory and Alex Ruzicka for providing a sample of Fitzwater Pass, and Northern Arizona University for lending Zinder, and Ted Bunch for lending NWA 1911. We are grateful to AE Thorsten Kleine for handling the manuscript and reviewers Alex Ruzicka, Emily Worsham, Ed Scott, and Alfred Kracher for their comprehensive and constructive reviews on this work. This work was supported by NASA Grants 80NSSC19K1238 (BZ), 80NSSC19K1613 (NLC), 80NSSC18K0595 (MH) and NNX17AE77G (AER). A portion of this work was performed at the National High Magnetic Field Laboratory, which is supported by the National Science Foundation Cooperative Agreement No. DMR-1644779 and the State of Florida.

APPENDIX A. SUPPLEMENTARY MATERIAL

Supplementary data to this article can be found online at https://doi.org/10.1016/j.gca.2022.02.004.

REFERENCES

Antonelli M. A., Kim S. T., Peters M., Labidi J., Cartigny P., Walker R. J., Lyons J. R., Hoek J. and Farquhar J. (2014) Early inner solar system origin for anomalous sulfur isotopes in differentiated protoplanets. *Proc. Natl. Acad. Sci. USA* **111**, 17749–17754.

Boesenberg J. S., Humayun M. and Van Niekerk D. (2017) Zinder: The first mantle sample from the IIIF iron parent body. In *In Lunar and Planetary science conference*, p. 2319.

Boesenberg J. S., Davis A. M., Prinz M., Weisberg M. K., Clayton R. N. and Mayeda T. K. (2000) The pyroxene pallasites, Vermillion and Yamato 8451: Not quite a couple. *Meteorit. Planet. Sci.* **35**, 757–769.

Boesenberg J. S., Delaney J. S. and Hewins R. H. (2012) A petrological and chemical reexamination of Main Group pallasite formation. *Geochim. Cosmochim. Acta* **89**, 134–158.

Boesenberg J. S., Mayne R. G., Humayun M., Silver A. P., Greenwood R. C. and Franchi I. A. (2016) Pyroxene-plagioclase pallasite Northwest Africa 10019: Where does it belong?. *In 47th Lunar and planetary science conference*.

Buchwald W. F. (1975) Handbook of Iron Meteorites: Their History, Distribution, Composition, and Structure. University of California Press, Berkeley.

Bunch T. E., Rumble, III, D., Wittke J. H. and Irving A. J. (2005) Pyroxene-rich pallasites Zinder and NWA 1911: Not like the others. *Meteorit. Planet. Sci. Supplement* **40**, 5219.

Campbell A. J. and Humayun M. (2005) Compositions of group IVB iron meteorites and their parent melt. *Geochim. Cosmochim. Acta* **69**, 4733–4744.

Chabot N. L. (2004) Sulfur contents of the parental metallic cores of magmatic iron meteorites. *Geochim. Cosmochim. Acta* **68**, 3607–3618.

Chabot N. L., Wollack E. A., McDonough W. F., Ash R. D. and Saslow S. A. (2017) Experimental determination of partitioning in the Fe-Ni system for applications to modeling meteoritic metals. *Meteorit. Planet. Sci.* **52**, 1133–1145.

Chabot N. L. and Zhang B. (2021) A revised trapped melt model for iron meteorites applied to the IIIAB group. *Meteorit. Planet. Sci.*. doi.10.1111/maps.13740.

Cohen E. (1905) Meteoritenkunde, Heft III. Schweizerbart'sche Verlagshandiung, Stuttgart.

Glass B. P. (1990) Tektites and microtektites: Key facts and inferences. *Tectonophysics* **171**, 393–404.

Clayton R. N. and Mayeda T. K. (1996) Oxygen isotope studies of achondrites. *Geochim. Cosmochim. Acta* **60**, 1999–2017.

Goldberg E., Uchiyama A. and Brown H. (1951) The distribution of nickel, cobalt, gallium, palladium and gold in iron meteoites. *Geochim. Cosmochim. Acta* **2**, 1–25.

Gregory J. D., Mayne R. G., Boesenberg J. S., Humayun M., Silver A. P., Greenwood R. C. and Franchi I. A. (2016) Choteau makes three: A characterization of the third member of the Vermillion subgroup. *In 47th Lunar and planetary science conference*.

Hilton C. D., Ash R. D. and Walker R. J. (2022) Chemical characteristics of iron meteorite parent bodies. *Geochim. Cosmochim. Acta* **318**, 112–125.

Grewal D. S., Dasgupta R. and Marty B. (2021) A very early origin of isotopically distinct nitrogen in inner Solar System protoplanets. *Nat. Astron.* **5**, 356–364.

Hilton C. D., Ash R. D. and Walker R. J. (2020) Crystallization histories of the group IIF iron meteorites and Eagle Station pallasites. *Meteorit. Planet. Sci.* **55**, 2570–2586.

Humayun M. (2012) Chondrule cooling rates inferred from diffusive profiles in metal lumps from the Acfer 097 CR2 chondrite. *Meteorit. Planet. Sci.* **47**, 1191–1208.

Humayun M., Boesenberg J. S. and van Niekirk D. (2018) Composition of the IIIF irons and their relationship to the Zinder pallasite. In *In 49th Lunar and planetary science conference*, p. 1461.

Kracher A., Willis J. and Wasson J. T. (1980) Chemical classification of iron meteorites—IX. A new group (IIF), revision of IAB and IIICD, and data on 57 additional irons. *Geochim. Cosmochim. Acta* **44**, 773–787.

Kruijer T. S., Burkhardt C., Budde G. and Kleine T. (2017) Age of Jupiter inferred from the distinct genetics and formation times of meteorites. *Proc. Natl. Acad. Sci. USA* **114**, 6712–6716.

Kruijer T. S. and Kleine T. (2019) Age and origin of IIE iron meteorites inferred from Hf-W chronology. *Geochim. Cosmochim. Acta* **262**, 92–103.

Kruijer T. S., Kleine T. and Borg L. E. (2019) The great isotopic dichotomy of the early Solar System. *Nat. Astron.* **4**, 1–9.

Lovering J. F., Nichiporuk W., Chodos A. and Brown H. (1957) The distribution of gallium, germanium, cobalt, chromium, and copper in iron and stony-iron meteorites in relation to nickel content and structure. *Geochim. Cosmochim. Acta* **11**, 263–278.

Massalski T. and Subramanian P. R. (1990) Binary Alloy Phase Diagrams, 2nd ed. ASM international, Materials Park, Cleveland.

McDonough W. F. and Sun S.-S. (1995) The composition of the Earth. *Chem. Geol.* **120**, 223–253.

Merrill G. P. (1927) A recently found iron meteorite from Oakley, Idaho. *Proc. U. S. Natl. Mus.* **71**, 1–6.

Moore C. B., Lewis C. F. and Nava D. (1969) Superior analyses of iron meteorites. In *Meteorite research*. Springer, pp. 738–748.

Pernicka E. and Wasson J. T. (1987) Ru, Re, OS, Pt and Au in iron meteorites. *Geochim. Cosmochim. Acta* **51**, 1717–1726.

Peters S., Jackson T., Chakraborty S., Almeida N. and Thiemens M. (2020) Tracing the nebular snowline with sulfur isotopes in iron meteorites. In *In Lunar and planetary science conference*, p. 1939.

Pouchou J.-L. and Pichoir F. (1991) Quantitative analysis of homogeneous or stratified microvolumes applying the model "PAP". In *Electron Probe Quantitation*. Springer, pp. 31–75.

Prombo C. A. and Clayton R. N. (1993) Nitrogen isotopic compositions of iron meteorites. *Geochim. Cosmochim. Acta* **57**, 3749–3761.

Qin L., Dauphas N., Wadhwa M., Masarik J. and Janney P. E. (2008) Rapid accretion and differentiation of iron meteorite parent bodies inferred from ^{182}Hf–^{182}W chronometry and thermal modeling. *Earth Planet. Sci. Lett.* **273**, 94–104.

Schaudy R., Watson J. T. and Buchwald V. F. (1972) The chemical classification of iron meteorites. VI. A reinvestigation of irons with Ge concentration lower than 1 ppm. *Icarus* **17**, 174–192.

Scott E. R. (2020) Iron Meteorites: Composition, Age, and Origin. *Oxford Research Encyclopedia of Planetary Science*. Oxford University.

Scott E. R. and Wasson J. T. (1976) Chemical classification of iron meteorites—VIII. Groups IC. IIE, IIIF and 97 other irons. *Geochim. Cosmochim. Acta* **40**, 103–115.

Spitzer F., Burkhardt C., Budde G., Kruijer T. and Kleine T. (2020) Isotopic evolution of the protoplanetary disk as recorded in Mo isotopes of iron meteorites. In *In Lunar and planetary science conference*, p. 3040.

Spitzer F., Burkhardt C., Nimmo F. and Kleine T. (2021) Nucleosynthetic Pt isotope anomalies and the Hf-W chronology of core formation in inner and outer solar system planetesimals. *Earth Planet Sci. Lett.* **576**, 117211.

Sunshine J. M., Bus S. J., Corrigan C. M., McCoy T. J. and Burbine T. H. (2007) Olivine-dominated asteroids and meteorites: Distinguishing nebular and igneous histories. *Meteorit. Planet. Sci.* **42**, 155–170.

Tornabene H. A., Hilton C. D., Bermingham K. R., Ash R. D. and Walker R. J. (2020) Genetics, age and crystallization history of group IIC iron meteorites. *Geochim. Cosmochim. Acta* **288**, 36–50.

Walker R. J., McDonough W. F., Honesto J., Chabot N. L., McCoy T. J., Ash R. D. and Bellucci J. J. (2008) Modeling fractional crystallization of group IVB iron meteorites. *Geochim. Cosmochim. Acta* **72**, 2198–2216.

Wasson J. T. (1999) Trapped melt in IIIAB irons; solid/liquid elemental partitioning during the fractionation of the IIIAB magma. *Geochim. Cosmochim. Acta* **63**, 2875–2889.

Wasson J. T. (2003) Large aerial bursts: An important class of terrestrial accretionary events. *Astrobiology* **3**, 163–179.

Wasson J. T. (2016) Formation of the Treysa quintet and the main-group pallasites by impact-generated processes in the IIIAB asteroid. *Meteorit. Planet. Sci.* **51**, 773–784.

Wasson J. T. and Choe W.-H. (2009) The IIG iron meteorites: Probably formation in the IIAB core. *Geochim. Cosmochim. Acta* **73**, 4879–4890.

Wasson J. T. and Choi B.-G. (2003) Main-group pallasites: Chemical composition, relationship to IIIAB irons, and origin. *Geochim. Cosmochim. Acta* **67**, 3079–3096.

Wasson J. T. and Huber H. (2006) Compositional trends among IID irons; their possible formation from the P-rich lower magma in a two-layer core. *Geochim. Cosmochim. Acta* **70**, 6153–6167.

Wasson J. and Richardson J. (2001) Fractionation trends among IVA iron meteorites: Contrasts with IIIAB trends. *Geochim. Cosmochim. Acta* **65**, 951–970.

Wasson J. T., Huber H. and Malvin D. J. (2007) Formation of IIAB iron meteorites. *Geochim. Cosmochim. Acta* **71**, 760–781.

Wasson J. T. and Kimberlin J. (1967) The chemical classification of iron meteorites—II. Irons and pallasites with germanium concentrations between 8 and 100 ppm. *Geochim. Cosmochim. Acta* **31**, 2065–2093.

Wasson J. T., Ouyang X., Wang J. and Eric J. (1989) Chemical classification of iron meteorites: XI. Multi-element studies of 38 new irons and the high abundance of ungrouped irons from Antarctica. *Geochim. Cosmochim. Acta* **53**, 735–744.

Wasson J. T. and Kallemeyn G. W. (2002) The IAB iron-meteorite complex: A group, five subgroups, numerous grouplets, closely related, mainly formed by crystal segregation in rapidly cooling melts. *Geochim. Cosmochim. Acta* **66**, 2445–2473.

Worsham E. A., Bermingham K. R. and Walker R. J. (2017) Characterizing cosmochemical materials with genetic affinities to the Earth: genetic and chronological diversity within the IAB iron meteorite complex. *Earth Planet. Sci. Lett* **467**, 157–166.

Worsham E. A., Burkhardt C., Budde G., Fischer-Gödde M., Kruijer T. S. and Kleine T. (2019) Distinct evolution of the carbonaceous and non-carbonaceous reservoirs: Insights from Ru, Mo, and W isotopes. *Earth Planet. Sci. Lett.* **521**, 103–112.

Associate editor: Thorsten Kleine